Circulation Induced by Isolated Dense Water Formation over Closed Topographic Contours

MICHAEL A. SPALL, JOSEPH PEDLOSKY, AND CLAUDIA CENEDESE

Woods Hole Oceanographic Institution, Woods Hole, Massachusetts

(Manuscript received 1 March 2017, in final form 30 June 2017)

ABSTRACT

The problem of localized dense water formation over a sloping bottom is considered for the general case in which the topography forms a closed contour. This class of problems is motivated by topography around islands or shallow shoals in which convection resulting from brine rejection or surface heat loss reaches the bottom. The focus of this study is on the large-scale circulation that is forced far from the region of surface forcing. The authors find that a cyclonic current is generated around the topography, in the opposite sense to the propagation of the dense water plume. In physical terms, this current results from the propagation of low sea surface height from the region of dense water formation anticyclonically along the topographic contours back to the formation region. This pressure gradient is then balanced by a cyclonic geostrophic flow. This basic structure is well predicted by a linear quasigeostrophic theory, a primitive equation model, and in rotating tank experiments. For sufficiently strong forcing, the anticyclonic circulation of the dense plume meets this cyclonic circulation to produce a sharp front and offshore advection of dense water at the bottom and buoyant water at the surface. This nonlinear limit is demonstrated in both the primitive equation model and in the tank experiments.

1. Introduction

Dense water formation by air–sea interaction is a key process that sets the properties of the ocean's water masses and represents an important exchange of heat and/or freshwater between the ocean and atmosphere or cryosphere. Water may become denser by losing heat to the atmosphere, evaporation to the atmosphere, or through brine rejection by the formation of sea ice (effectively removing freshwater from the ocean). These processes take place in many places throughout the World Ocean.

There are a few locations in which buoyancy loss in the open ocean results in deep convection and the formation of large volumes of identifiable water masses or mode waters. Well-studied regions of deep-water formation include the Labrador Sea, the Greenland Sea, and the Mediterranean Sea (Marshall and Schott 1999). These locations are characterized by weak stratification, weak mean flows, and large-scale atmospheric forcing. The buoyancy loss in the region of deep convection is largely compensated for by lateral buoyancy fluxes carried by baroclinic eddies (Marshall and Schott 1999; Visbeck et al. 1996; Spall 2004).

Dense water formation is also found in the vicinity of islands, such as Wrangle Island (Moore and Pickart 2012), St. Lawrence Island (Danielson et al. 2006), and Svalbard (Skogseth et al. 2008). In these cases, the forcing tends to be much more localized than for open-ocean convection because the atmospheric forcing varies on smaller scales due to the island orography or polynyas that form in the island lee. Although these islands are relatively small compared to planetary scale, the Weddell Sea, along the perimeter of Antarctica, is also a well-known location of dense water formation.

A key dynamical difference between dense water formation near islands and that in the open ocean is that near the islands the convection is likely to penetrate to the bottom. This is important because the topography around islands closes upon itself, forming pathways of closed f/h contours, where f is the Coriolis parameter, and h is the bottom depth. It is well known that forcing on closed f/h contours can drive strong, large-scale flows well away from the region of forcing (Welander 1968; Young and Rhines 1982). Although the dynamics are broadly relevant to deep basins and shoals with closed contours, the present focus is on islands because the atmospheric forcing is often more localized and, near the island, convection is likely to reach the bottom. Spall (2013) considered the case of uniform cooling

Corresponding author: Michael Spall, mspall@whoi.edu

DOI: 10.1175/JPO-D-17-0042.1

around islands and demonstrated that the azimuthally averaged circulation was controlled by a balance of lateral eddy fluxes and air–sea exchange near the island. For the present study, we instead focus on the circulation resulting from asymmetric forcing over closed f/h contours.

We apply three different methods to address the ocean response to localized dense water formation over closed topographic contours. A quasigeostrophic (QG) theory is developed in section 2 that demonstrates the basic response to asymmetric forcing and highlights the nonlocal nature of the circulation. In section 3, these physics are reproduced and then extended into a regime more representative of strong, episodic dense water formation using a primitive equation model. Finally, in section 4, a series of experiments are carried out in a rotating tank that demonstrates similar behavior without parameterizations of turbulent mixing.

2. Linear steady theory

a. Formulation

We consider in this section a linear model for the steady-state circulation over a conical topographic feature. The model is quasigeostrophic and has the advantages and disadvantages of such a theory; that is, the model is easily analyzed but is idealized and limited in fundamental ways, not least being that the elevation of the topographic feature must be small compared to the total fluid depth D. The isolated topography is chosen to be a cone of radius r_0. As we shall see, the precise height of the cone is inconsequential as long as it is greater than the Ekman layer thickness. In quasigeostrophic theory, the topographic height must also be small by order Rossby number when compared to D.

The governing equations for momentum and mass are linear, Boussinesq, and hydrostatic, and the dissipation is modeled by simple vertical mixing with a turbulent vertical mixing coefficient A. Otherwise the notation is standard. In cylindrical polar coordinates,

$$fu = -\frac{1}{r}\frac{\partial \phi}{\partial \theta} + A\frac{\partial^2 v}{\partial z^2}, \tag{1a}$$

$$-fv = -\frac{\partial \phi}{\partial r} + A\frac{\partial^2 u}{\partial z^2}, \tag{1b}$$

$$\frac{1}{r}\frac{\partial ru}{\partial r} + \frac{1}{r}\frac{\partial v}{\partial \theta} = -\frac{\partial w}{\partial z}, \quad \text{and} \tag{1c}$$

$$\frac{\rho g}{\rho_0} = -\frac{\partial \phi}{\partial z}, \tag{1d}$$

where u and v are the radial and azimuthal velocity components, while w is the vertical velocity. The function ϕ is the pressure field divided by the mean background density ρ_0, z is the vertical coordinate, and r is the radial coordinate. The layer of fluid is contained between $0 \le z \le D$. Here, ρ is the density anomaly with regard to the background.

The fluid is driven by heating and cooling such that the rate of change of the density is determined by a heating/cooling function Q. The principal approximation in the model is that the equation for density can be simplified to a balance between Q and the vertical motion of the fluid in a background, uniform density gradient $\partial\overline{\rho}/\partial z = -\rho_0 N^2/g$, where the overbar indicates the horizontal average over the domain. Thus,

$$w\frac{\partial \overline{\rho}}{\partial z} = -\gamma(\rho - \rho_*) = Q, \tag{2}$$

or

$$w = \frac{\gamma g}{\rho_0 N^2}(\rho - \rho_*), \tag{3}$$

where $\rho_*(r, \theta, z)$ is the target density anomaly to which the density field is driven by the heating and cooling. The constant γ is the inverse relaxation time constant for the density to reach the target.

In the analysis that follows, it is useful to put the equations in nondimensional form. The topographic cone's radius r_0 is used to scale horizontal lengths, and D is used for vertical lengths. The density anomaly is scaled by $\Delta\rho_H$, the amplitude of the target density anomaly, in terms of which the velocity scale is $U = gD\Delta\rho_H/\rho_0 fr_0$ with a corresponding scale for ϕ of $g\Delta\rho_H D/\rho_0$. The vertical velocity scale is UD/r_0.

In these units the governing equations become

$$u = -\frac{1}{r}\frac{\partial \phi}{\partial \theta} + \frac{E_v}{2}\frac{\partial^2 v}{\partial z^2}, \tag{4a}$$

$$-v = -\frac{\partial \phi}{\partial r} + \frac{E_v}{2}\frac{\partial^2 u}{\partial z^2}, \tag{4b}$$

$$\frac{1}{r}\frac{\partial ru}{\partial r} + \frac{1}{r}\frac{\partial v}{\partial \theta} = -\frac{\partial w}{\partial z}, \tag{4c}$$

$$\rho = -\frac{\partial \phi}{\partial z}, \quad \text{and} \tag{4d}$$

$$w = \frac{\gamma}{fS}(\rho - \rho_*), \tag{4e}$$

where $E_v = 2A/fD^2$, which we will assume is a very small parameter, and $S = N^2D^2/f^2r_0^2$.

The lower boundary is slightly raised by the topography but in quasigeostrophic theory the boundary condition is applied at $z = 0$. The presence of an Ekman

layer to satisfy the no-slip condition yields the lower boundary condition (Pedlosky 1987):

$$w(r,\theta,0) = \frac{E_v^{1/2}}{2}\zeta(r,\theta,0) + u\frac{\partial h_b}{\partial r}. \tag{5}$$

In (5) the topographic height has been scaled by D, and ζ is the vertical component of the relative vorticity, that is,

$$\zeta = \frac{1}{r}\frac{\partial rv}{\partial r} - \frac{1}{r}\frac{\partial u}{\partial \theta}.$$

At the upper surface we will apply a no stress condition. The required Ekman layer at the upper surface is weaker and gives rise to the boundary condition for the interior flow in the form (Pedlosky 1987)

$$w(r,\theta,1) = -\frac{E_v}{2}\frac{\partial \zeta}{\partial z}. \tag{6}$$

From the momentum equations it can easily be shown that the horizontal divergence of the velocity is order E_v so that $\partial w/\partial z$ is also of that smallness. This implies that the interior w will be of that order, and for consistency it follows that the ratio $\gamma/f = O(E_v)$. A central parameter governing the dynamics in this model will be the ratio

$$\lambda = \frac{2\gamma}{fE_vS}. \tag{7}$$

The condition that λ is order one implies that the two estimates of the vertical velocity, (5) and (6), are consistent for horizontal scales of the topography r_0 on the order of the deformation radius ND/f, that is, the parameter S is assumed to be $O(1)$.

Note that for the axially symmetric part of the flow field, the geostrophic radial velocity will be zero, and the ageostrophic radial velocity in the interior is only $O(E_v)$. However, if there is an azimuthal mean velocity at $z = 0$, the lower Ekman layer would yield an order $E_v^{1/2}$ radial mass flux. That mass flux would lead to a singularity in the mass flux at the origin. Hence, for the azimuthal mean portion of the solution, the azimuthal mean of v must be zero at the lower boundary.

Calculating the horizontal divergence of the velocity from the momentum equations yields

$$\frac{E_v}{2}\frac{\partial^2 \zeta}{\partial z^2} = -\frac{\partial w}{\partial z} = -\frac{E_v}{2}\lambda\frac{\partial}{\partial z}(\rho - \rho_*). \tag{8}$$

Since $E_v\lambda$ is small, the vorticity can be evaluated geostrophically, while the density is related to the pressure field ϕ geostrophically, allowing (8) to be written as

$$\frac{\partial^2}{\partial z^2}(\nabla^2\phi - \lambda\phi) = \lambda\frac{\partial \rho_*}{\partial z}, \tag{9}$$

where the Laplacian in (9) is in the horizontal. The boundary conditions follow from (5) and (6) with the use of (3) and (4d).

b. *The axially symmetric portion of the solution*

The forcing of the motion is given in (9) by the target function $\rho_*(r, \theta, z)$. We define the azimuthal mean of that forcing as $\overline{\rho}_* = \overline{\rho}_*(r, z)$. For simplicity and analytic convenience, and to make the example concrete, we will choose the target density function to have the azimuthal mean

$$\overline{\rho}_*(r,z) = (1 - r^2)\sinh(\mu z) \tag{10}$$

for $r \le 1$ and zero for $r > 1$. In (10), μ is the inverse length scale of the vertical variation of the target density and is $O(1)$.

For that functional form of the forcing the general solution of (9) for the azimuthal mean is

$$\overline{\phi} = \frac{\cosh\mu z}{\lambda\mu}\left[4 - \lambda(1 - r^2) + C_1\frac{I_0(\lambda^{1/2}r)}{I_0(\lambda^{1/2})}\right] + Az + B, \tag{11}$$

where A and B are arbitrary functions of r, C_1 is a constant (defined below), and $I_0(\lambda^{1/2}r)$ is the modified Bessel function of the first kind and is regular at $r = 0$. The solution (11) is valid for $0 \le r \le 1$. For $r > 1$, where the target density anomaly is zero, the solution is

$$\overline{\phi} = \frac{\cosh\mu z}{\lambda\mu}\frac{K_0(\lambda^{1/2}r)}{K_0(\lambda^{1/2})} + \alpha z + \beta, \tag{12}$$

where K_0 is a modified Bessel function of the second kind, and α and β are functions only of r.

As shown before, it is necessary that the azimuthal velocity vanish on $z = 0$. At the same time, the solutions (11) and (12) already satisfy the boundary condition at $z = 1$. The Ekman layer on the upper surface required to satisfy the no stress condition yields the standard matching condition for the geostrophic flow given by (6). When combined with (5), this yields for the azimuthal mean and any deviation from the mean

$$\frac{\partial}{\partial z}(\nabla^2\phi - \lambda\phi) = \lambda\rho_*. \tag{13}$$

It is clear that the solution of (9), as derived in (11), will automatically satisfy (13). Thus, we obtain

$$\overline{\phi} = \frac{\cosh\mu z - 1}{\lambda\mu} \begin{cases} 4 - \lambda(1 - r^2) + C_1 \dfrac{I_0(\lambda^{1/2} r)}{I_0(\lambda^{1/2})} & 0 \le r \le 1 \\ C_2 \dfrac{K_0(\lambda^{1/2} r)}{K_0(\lambda^{1/2})} & r > 1 \end{cases}. \tag{14}$$

It remains to apply the continuity conditions for $\overline{\phi}$ and its radial derivative at $r = 1$. Those conditions lead to the determination of C_1 and C_2, namely,

$$C_1 = -2 \frac{\lambda^{1/2} + 2\dfrac{K_1(\lambda^{1/2})}{K_0(\lambda^{1/2})}}{\dfrac{I_1(\lambda^{1/2})}{I_0(\lambda^{1/2})} + \dfrac{K_1(\lambda^{1/2})}{K_0(\lambda^{1/2})}}, \quad C_2 = C_1 + 4, \tag{15}$$

while the azimuthal mean of the azimuthal velocity $\overline{v}$ is given by

$$\overline{v} = \frac{\cosh\mu z - 1}{\mu\lambda} \begin{cases} \left[2r\lambda + C_1 \lambda^{1/2} \dfrac{I_1(\lambda^{1/2} r)}{I_0(\lambda^{1/2})} \right], & r \le 1 \\ -\lambda^{1/2} C_2 \dfrac{K_1(\lambda^{1/2} r)}{K_0(\lambda^{1/2})}, & r > 1 \end{cases}. \tag{16}$$

Note that it follows from (4a)–(4e), (8), and (9) and the fact that both $\partial\overline{\phi}/\partial z$ and ρ_* vanish on $z = 0$ that

$$\overline{w} = \frac{\partial \nabla^2 \overline{\phi}}{\partial z}, \tag{17}$$

and hence, since $\overline{\phi}$ vanishes at infinity exponentially fast as long as λ is not zero, it follows that the area integral of the vertical velocity over the domain must vanish. Before examining the nature of the mean azimuthal circulation in detail, we first consider the problem for the deviation from the mean in θ.

c. Deviation from the azimuthal mean

The deviation from the axial mean of the forcing target density anomaly could have a complicated structure, but for illustrative purposes we will consider a forcing in addition to the axial mean of the form

$$\rho_{*n} = \rho_n J_n(kr) \sinh(\mu z) \cos(n\theta) \tag{18}$$

for $r \le 1$ and zero for $r > 1$. In (18) we have chosen k to be the first zero of the Bessel function of nth order, which gives the radial form of the forcing. The forcing is therefore limited to the region above the topographic cone. The governing equation for this portion of the solution is, again, (9) with the target density given by (18). Since the problem is linear, the solution of (18) can be simply added to the previous solution [(14)]. Arbitrary forcing can be represented by a double Fourier series of trigonometric functions in θ and a Bessel series in r, but we will restrict attention to forcing by a single term to keep things as simple as possible. The general solution in the region can be found as

$$\phi_n = \cos n\theta \begin{cases} zA_n + B_n + \cosh\mu z \left[-\dfrac{\lambda}{\mu(\lambda + k^2)} J_n(kr) + C_3 \dfrac{I_n(\lambda^{1/2} r)}{I_n(\lambda^{1/2})} \right] & r \le 1 \\ z\alpha_n + \beta_n + C_4 \cosh\mu z \dfrac{K_n(\lambda^{1/2} r)}{K_n(\lambda^{1/2})} & r > 1 \end{cases}. \tag{19}$$

As before, the functions A_n, B_n, α_n, and β_n are functions of the horizontal coordinates r, and C_3 and C_4 are constants, defined below. The boundary condition at $z = 0$ is (5), that is,

$$w_n = \frac{1}{2}\lambda E_v(\rho - \rho_n) = \frac{1}{2} E_v^{1/2} \zeta_n + u_n \frac{\partial h_b}{\partial r}. \tag{20}$$

Note again that the subscript n refers to the solution proportional to the nth Fourier mode in θ. The topographic elevation must be small in quasigeostrophic theory, so the term $\partial h_b/\partial r$ is small with respect to one. Note that that term has been scaled by D/r_0. Nevertheless, we expect the topographic relief to be greater than the Ekman layer thickness on the lower boundary so that the topographic term in (20) will be dominant. In turn that implies that the radial velocity must itself vanish on $z = 0$. But this in turn implies that to the lowest order the streamfunction in this mode must be zero at $z = 0$.

Again, as in the previous section, the solution as given automatically satisfies the boundary condition on $z = 1$. Note that the condition that the velocity vanish at $z = 0$ eliminates both β_n and B_n. The function $A(r)$ can be easily shown to satisfy the homogeneous form of (13). The solution of that problem with homogeneous boundary conditions must be zero.

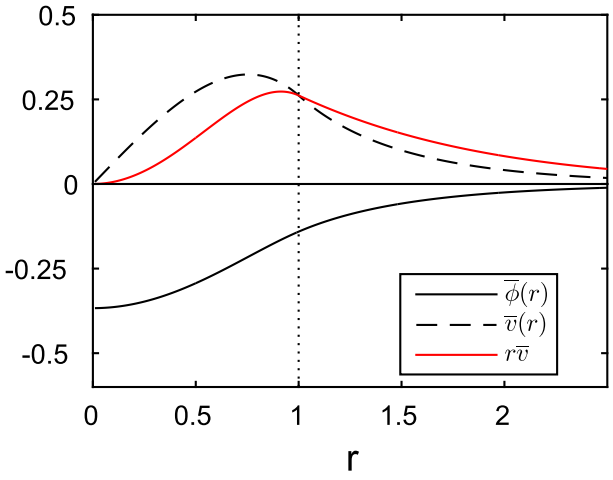

FIG. 1. Azimuthal mean solution for the linear quasigeostrophic theory.

That condition and the aforementioned boundary condition on $z = 1$, along with the continuity conditions on the streamfunction and its radial derivative at $r = 1$, leads to the final solution for ϕ_n, that is, for C_3, C_4 in (19):

$$C_3 = C_4 = \frac{-\dfrac{\rho_n \lambda k}{\mu(\lambda + k^2)} J_{n+1}(k)}{\lambda^{1/2}\left[\dfrac{I_{n+1}(\lambda^{1/2})}{I_n(\lambda^{1/2})} + \dfrac{K_{n+1}(\lambda^{1/2})}{K_n(\lambda^{1/2})}\right]}. \qquad (21)$$

In this linear model, the magnitude of the bottom relief does not enter the solution for either the azimuthal mean or deviation, but the presence of the bottom topography is the cause of the flow vanishing on the lower boundary.

d. Results

Figure 1 shows the structure in r of the azimuthal mean of the solution. The z dependence of the velocity and geostrophic streamfunction is an exponentially increasing function of z starting with zero at the lower boundary. The solution presented in Fig. 1 has a target density anomaly given by (10). The case shown implies a positive value for the target anomaly representing a tendency for cooling. Note that the vertical velocity and hence the actual heating or cooling depends on the difference between the target and the achieved density perturbation. The cooling gives rise to a positive azimuthal velocity v shown by the dashed curve in the figure. The solid curve is the radial form of the streamfunction $\overline{\phi}$ for the azimuthal mean. The red curve shows the product $r\overline{v}$, which, aside from a factor of 2π, is the circulation. The circulation in turn is a measure of the area-integrated relative vorticity in the region less than r. From (8) and the exponential structure in z, it follows that the circulation gives us the area integral of the downward vertical velocity flux in the region within r. As the figure shows, the vertical mass flux is negative at small r, where the cooling is strongest, and the integrated total diminishes at larger r, where a compensating positive vertical velocity occurs when the density anomaly locally exceeds the target. At values of r much greater than $\lambda^{-1/2}$, the response of the fluid is negligible, showing that complete compensation in the vertical circulation occurs over that scale. In dimensional units, this decay scale is $L_d(fE_v/2\gamma)^{1/2} = O(L_d)$, where $L_d = ND/f$ is the baroclinic deformation radius.

The response of the deviation from the azimuthal mean is somewhat smaller than the mean, even if the amplitude of the target density anomaly is the same. This reflects both the different radial forms for the target densities as well as the tendency of the operator for the deviation to yield smaller amplitudes for the same level of forcing.

The forcing considered here has an azimuthal mean part given by (10) with amplitude unity at the center of the topographic cone, diminishing parabolically to zero at the edge of the cone. The azimuthal variable part of the forcing goes like $\cos\theta$ so that n in (18) is one. The maximum value of the Bessel function in the range of the topography is about 0.6, so the amplitude of this portion of the forcing was chosen to be -2 to give it a size of the same order as the mean forcing. The negative value means that the cooling is maximum on the left (west) side of the topographic cone. It is important to note that the radial structure of the two components of the forcing, chosen to allow simple analytical solutions, is different so there is not an exact correspondence to the forcing in the numerical experiments discussed below.

The total geostrophic streamfunction shows a cyclonic circulation that is offset to the west of the topographic cone (Fig. 2a). There is northward flow over the eastern side of the topography but also over the western side in shallow water. The southward return flow is concentrated over the outer topographic slope to the west but also extends a distance that is $O(\lambda^{-1/2})$ outside the region of topography. The horizontal velocity, for $\lambda = O(1)$, will scale as $(g'D)^{1/2}$, where g' is the reduced gravity, while the horizontal transport streamfunction scales as $g'D^2/f$. These scalings will be tested in the numerical model and laboratory experiments in the following sections.

The vertical velocity is downward everywhere over the topographic slope and weakly upward outside the topography (Fig. 2b). The sinking is strongest over the

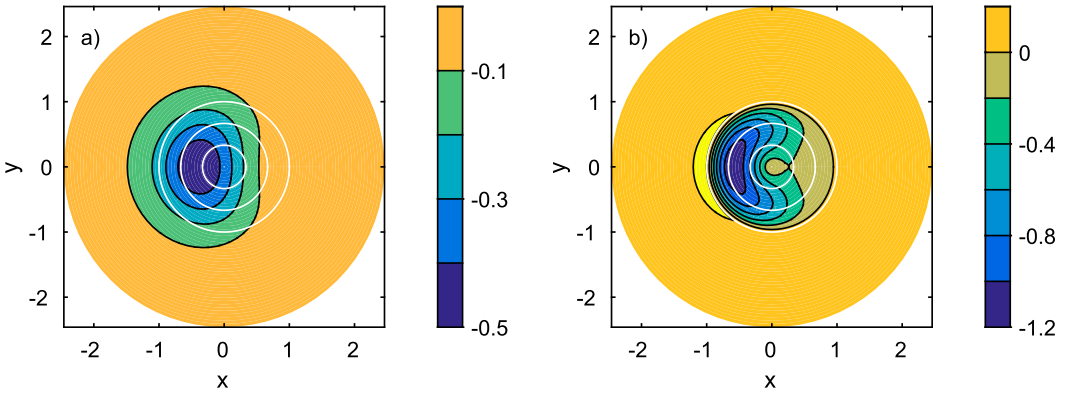

FIG. 2. (a) Total geostrophic transport streamfunction and (b) vertical velocity for the linear QG theory. White contours indicate the bottom topography.

western flank where the cooling is largest. Recall that the vertical velocity is proportional to the density anomaly, so this distribution also reflects the perturbation density due to the buoyancy forcing. As noted in the discussion of Fig. 1, the vertical velocity is of two signs. It is relatively large and negative in the region under the direct forcing and is upward and small at larger radius so that the total vertical mass flux is balanced. Since the dynamics are linear, the case of heating is the same solution with a simple change of sign. The net vertical flux of the deviatoric part of the solution is identically zero at each radius. The abrupt transition in w at the edge of the topography is related to the discontinuity of the vorticity gradient at that point.

3. Numerical model

The linear theory presented in the previous section provides closed-form solutions for the density distribution and velocity resulting from dense water formation over closed topographic contours. The dominant characteristic is an asymmetric cyclonic circulation that is shifted toward the region of dense water formation. In this section, we seek to connect this basic circulation pattern to that produced in a more complete model of buoyancy-forced flow over steep and shallow topography. These calculations are not intended to represent any specific oceanic region but instead are designed to exemplify space and time scales typical of dense water formation near islands.

We use the MIT general circulation model (MITgcm), which solves the hydrostatic primitive equations of motion on a Cartesian staggered C grid in the horizontal and fixed-depth coordinates in the vertical with a partial cell treatment of the bottom topography (Marshall et al. 1997). The problems are configured in a square domain 1440 km by 1440 km with a maximum bottom depth of 500 m. The horizontal grid spacing is 4 km and the vertical grid spacing is 25 m. The initial stratification is spatially uniform with $N^2 = 1.6 \times 10^{-6}\,\mathrm{s}^{-2}$. The Coriolis parameter is $10^{-4}\,\mathrm{s}^{-1}$ and constant. This gives a baroclinic deformation radius of $L_d = NH/f = 20$ km. Although the Coriolis parameter is constant, increasing y direction will be referred to as north and increasing x direction will be referred to as east in order to facilitate discussion of the results.

Subgrid-scale mixing is parameterized with a Smagorinsky deformation–dependent horizontal viscosity with nondimensional coefficient 2.5, Laplacian vertical viscosity, and vertical diffusivity with coefficients 10^{-2} and $10^{-6}\,\mathrm{m}^2\,\mathrm{s}^{-1}$, respectively. For statically unstable density profiles, the vertical diffusion is increased to $10^{3}\,\mathrm{m}^2\,\mathrm{s}^{-1}$ in order to represent vertical convection. There is also a linear bottom drag with coefficient 10^{-3}. The boundary conditions are no normal flow, no slip, and no temperature flux at the solid boundaries and no stress at the surface.

The model is configured and forced in two ways: In the first case, in order to compare with the linear theory, the topography is simply a cone that reaches up to a depth of 25 m at the middle of the domain and slopes linearly down to the flat-bottom depth of 500 m over a distance of $r_0 = 500$ km (slope $\alpha_T = 10^{-3}$). In these cases, the model is forced by restoring the temperature field toward a specified distribution $\overline{T}(z) + \Theta(r, \theta, z)$ with time scale $\gamma = 1/60$ days, where $\overline{T}(z)$ is the initial background temperature profile. The target temperature anomaly Θ varies radially from a maximum at the apex of the topography to zero at the outer radius of the topography as $1 - (r/r_0)^2$. For $r > r_0$, $\Theta = 0$. The forcing function also varies in the azimuthal direction such that it is a maximum on the western side of the topography and zero on the eastern side:

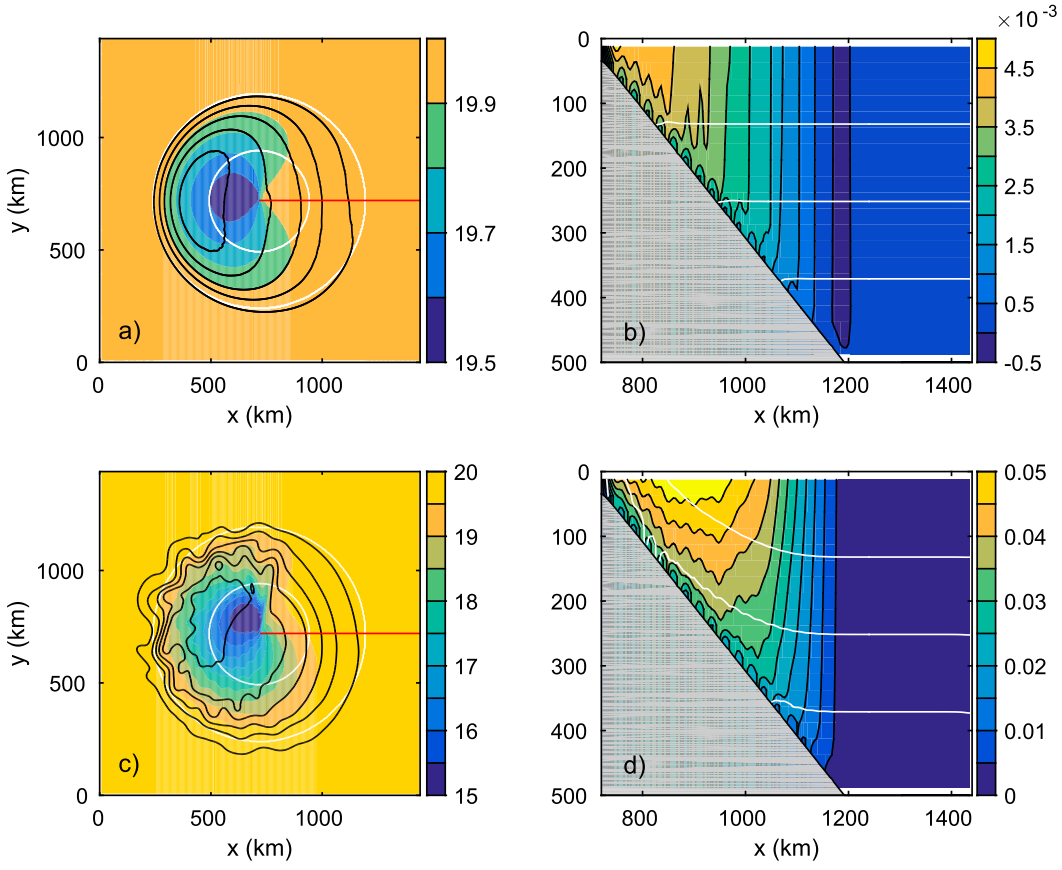

FIG. 3. (a) Sea surface temperature (colors), transport streamfunction (black contours, contour interval 0.05 Sv), and bottom topography (white contours at 250 and 500 m) for the case with $T' = -0.5$°C. (b) Vertical section of meridional velocity (colors) and temperature (white contours, contour interval 1°C) at the location indicated by the red line in (a). (c) As in (a), but for the case with $T' = -6$°C. (d) As in (b), but for the case with $T' = -6$°C.

$$\Theta = T'[1 - (r/r_0)^2][\cos(\theta) - 1]/2, \qquad (22)$$

where the maximum temperature anomaly is T'. The forcing function is applied uniformly in depth, mimicking deep convection that would result from buoyancy loss at the surface. This differs from the linear theory above primarily because imposing a nonzero buoyancy anomaly at the bottom would pose problems for the boundary conditions in the theory. Imposing a sinh structure in the vertical in the numerical model is not appropriate because the density anomaly over the shallow topography would not reach the maximum surface density, introducing unintended horizontal variability into the target density. Nonetheless, this forcing is similar in structure to that used for the linear theory and useful to test the general nature of the theoretical result. These differences make implementation easier in both the model and theory, and our findings of substantially similar results emphasize the robustness of the controlling dynamics.

The model is also configured with an island of radius $r_i = 200$ km in the middle of the domain, surrounded by a uniformly sloping bottom that extends from 25-m depth to 500-m depth with slope $\alpha_T = 1.5 \times 10^{-3}$. These calculations are forced with a heat flux at the surface given by $Q = \Gamma(T_a - T_1)$, where $T_a = 10$°C is an atmospheric temperature, T_1 is the model sea surface temperature (initially 20°C), and $\Gamma = 40\,\mathrm{W\,m^{-2}\,°C^{-1}}$ is a restoring constant. The surface cooling is applied in the sector $2.95 < |\theta|$ between $r_i < r < 320$ km for 60 days then turned off for 300 days, repeating every 360 days for 10 periods. This time-dependent forcing is intended to represent seasonal formation of dense water that results from buoyancy loss at the surface (either cooling or brine rejection) that is localized in space and time.

a. Conical topography with Θ forcing

The case with conical topography and temperature restoring with $T' = -0.5$°C produces a steady density field and circulation, as shown in Fig. 3a. The

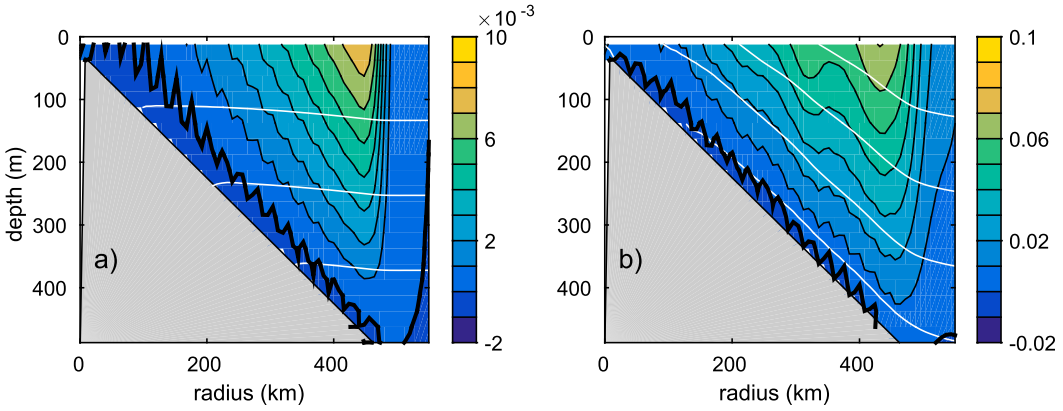

FIG. 4. Azimuthally averaged azimuthal velocity (colors) and temperature (white contours, contour interval 1°C) for (a) $T' = -0.5$°C and (b) $T' = -6$°C.

temperature anomaly is very similar to Θ. It has a minimum on the western side of the topography and decreases to zero in both the radial and azimuthal directions. The circulation is primarily cyclonic, but it does not coincide with the topographic contours. There is northward flow along the eastern flank of the topography but there is also northward flow over shallow water on the western flank. All of this northward flow returns to the south over the deep topography on the western edge of the cone. This is very similar to the circulation and density distribution found in the QG model (Fig. 2a). The center of this cyclonic recirculation is shifted to the west compared to the location of the coldest water. The circulation is of a sense to advect both the coldest water and the warmest water over the topography northward, although the forcing in this case is too weak for these nonlinear terms to be important in the density equation. However, based on the relationship between the horizontal velocity field and the temperature field, it is anticipated that there will be a horizontal heat flux convergence near $\theta = 90°$ (due north).

A section of the temperature and meridional velocity along the red line in Fig. 3a is shown in Fig. 3b. The velocity field is everywhere toward the north and nearly independent of depth. The velocity is maximum in shallow water and decreases to zero at the outer edge of the topography. Because the forcing is so weak, and $\Theta = 0$ at $\theta = 0$, the density field is essentially the same as the ambient stratification.

The influences of nonlinearity are indicated by a similar calculation with the perturbation temperature anomaly increased to $T' = -6$°C, as shown in Figs. 3c and 3d. The model is now time dependent and supports instabilities of the cyclonic flow around the dense water formation region. The mean sea surface temperature is similar to the linear case but, because of horizontal advection, asymmetries in the temperature field are now evident. On the western flank of the topography, the coldest water has been advected northward of the region of strongest cooling. The cold water has also been advected cyclonically around the island along the southern and eastern sectors so that cold water has penetrated beyond the midlatitude of the topography. The northward advection of cold water along the western flank and warm water along the eastern flank has produced a region of enhanced zonal temperature gradient near $\theta = 80°$, with an associated northward jet evident in the transport streamfunction, anticipated from the linear solution.

The zonal section of meridional velocity shows northward flow along the eastern flank (Fig. 3d); although there is now vertical shear that results in a surface-intensified flow. The vertical shear is caused by the dense water over the sloping topography. However, this dense water is not advected anticyclonically from the forcing region, in the direction of topographic wave propagation, as would be expected for a dense water plume. It is instead advected cyclonically from the south, as indicated in Fig. 3c.

In both cases, the flow along the eastern flank of the topography penetrates to the bottom. However, as shown in section 2, the azimuthally averaged velocity at the bottom is, to leading order, nearly zero. The azimuthally averaged velocity is a maximum near the surface and over deep water. This is the case for both the linear and nonlinear calculations discussed here (Fig. 4). At the bottom, the flow over the western flank of the topography is anticyclonic (dense water plume), while the flow over the east flank of the topography is cyclonic, as required to balance the circulation integral. This also sets up the frontogenetic condition that drives

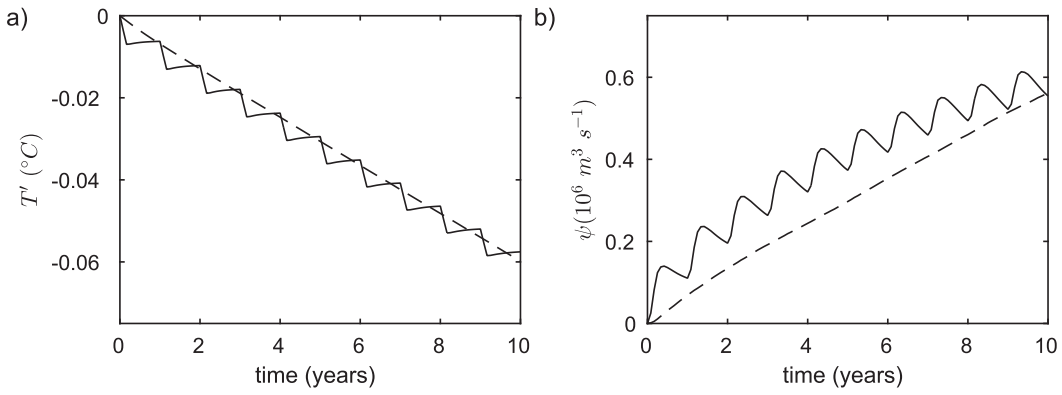

FIG. 5. (a) Basin-averaged temperature anomaly and (b) net transport around the island as a function of time for the case with seasonal surface forcing (solid) and constant forcing (dashed).

the confluence along the north flank of the topography and results in an abrupt offshore transport of the densest water (Fig. 3c).

b. Island topography with surface forcing

The MITgcm is now used to extend the analysis into configurations and forcing that are more representative of real dense water formation near islands. The cone is replaced with an island surrounded by sloping topography. The model is forced by an episodic heat flux at the surface that is proportional to the difference between the model sea surface temperature and an atmospheric temperature, as described above.

The basin-averaged temperature anomaly and the net transport around the island are shown as a function of time in Fig. 5. There are two inherent time scales. Dense water is formed and the circulation spins up rapidly on the seasonal forcing time scale. As will be shown below, the circumisland transport is achieved by the relatively fast propagation of the low sea surface height anomaly from the forcing region around the island. The rate of increase in the overall strength of the circulation around the topography slows over a longer, roughly decadal, time scale. If the model were run for a sufficiently long time, the ultimate equilibrium would be a motionless ocean at the atmospheric temperature since there is no source of heating to balance the surface cooling. However, given a source of heat we can anticipate that an equilibrium would be achieved in which there exists a cyclonic circulation around the island. Our interest here is not in the ultimate equilibrium solution, which will vary depending on the specifics of the topography and forcing, but instead on the existence of the cyclonic current. This long-term response to the cooling is not overly sensitive to the time scale of the forcing. A similar calculation with continual restoring to the atmospheric temperature with $\gamma = 1/180$ days (one-sixth of the previous restoring strength but applied for 6 times longer) shows very similar long-term evolution of both the basin-averaged temperature anomaly and transport around the island (Fig. 5, dashed line). The basic response to the surface cooling is revealed very quickly over the time scale of wave propagation. The repeated forcing cycle used here demonstrates that the basic response is maintained even over long times and intermittent forcing.

The temperature anomaly at the bottom, averaged over the final 2 years of the 10-yr integration, and the depth-integrated transport streamfunction are shown in Fig. 6a. These quantities are the difference between a calculation with surface forcing as described and an otherwise identical calculation with no surface forcing. The latter case generates temperature anomalies and currents because the no flux boundary condition on temperature, together with diffusion in the model, requires that the isopycnals be perpendicular to the sloping bottom topography. This results in vertical shear in the velocity field and drives an anticyclonic circulation around the island. This effect is subtracted out in Fig. 6, so these are the temperature and velocity anomalies driven by the surface cooling. The temperature anomaly also removes the background stratification so it is easier to see where the dense water is found.

The coldest water is found in the northwest quadrant, just north of the region of dense water formation (Fig. 6a). There is also a large-scale cyclonic circulation around the island. This current drives an upslope bottom Ekman layer, which has advected dense water upslope far from the region of surface forcing. The dense water from the convection region flows abruptly offshore where it meets with the cyclonic flow. The location of this separation point develops early in the calculation and then remains nearly constant for the duration of

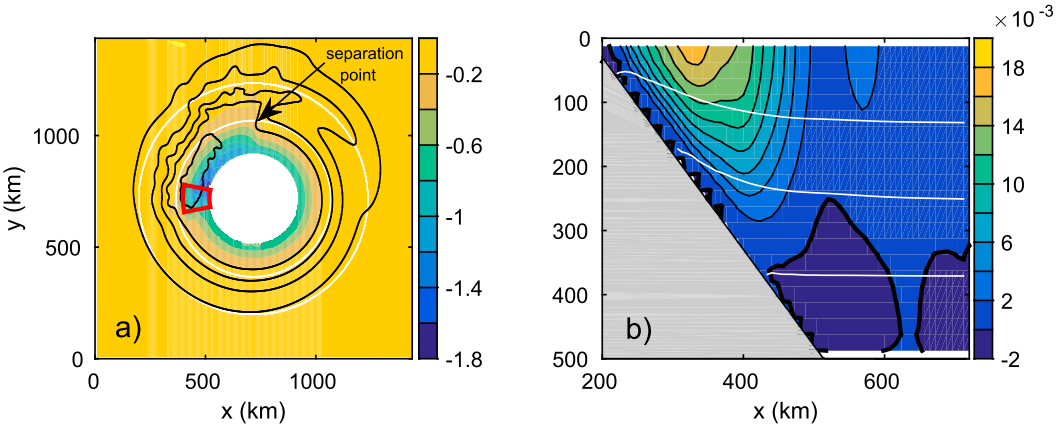

FIG. 6. (a) Mean bottom temperature anomaly (colors, °C), transport streamfunction (black contours, contour interval 0.1 Sv), and bottom topography (white contours depths 250 and 500 m). The region of surface cooling is indicated by the red box. (b) Azimuthally averaged azimuthal velocity (colors, thick black is zero contour) and temperature (white contours, contour interval 1°C).

the calculation so we interpret this as a steady aspect of the circulation.

The depth-integrated transport streamfunction reveals a predominantly cyclonic circulation around the topography of $O(0.5)$ Sv ($1\,\text{Sv} = 10^6\,\text{m}^3\,\text{s}^{-1}$). There is a small region of closed cyclonic recirculation to the west of the island, similar to that found in the more idealized calculations in the previous section. There is also evidence of the offshore pathway of the dense plume at the northern side of the topography and its continued extension anticyclonically around the island farther offshore (Fig. 6b).

The azimuthally averaged azimuthal velocity and temperature field demonstrate that the flow is dominated by a surface-intensified cyclonic circulation over the topography (Fig. 6b). Dense water is advected upslope near the bottom, causing a rise in the deep isotherms and vertical shear in the azimuthal velocity. The average velocity near the bottom is close to zero, as expected from the above theory and the circulation integral along topographic contours.

A series of calculations have been carried out with an identical geometry but with different values of the restoring constant for the surface heat flux Γ. For these calculations in which the mean sea surface temperature anomaly over the dense water formation region is small compared to the air–sea temperature difference, the net surface heat flux is nearly linearly proportional to Γ. The total density anomaly of the dense water formed is then approximately proportional to Γ. The maximum cyclonic velocity at the surface along the eastern flank of the island is plotted as a function of Γ in Fig. 7 (squares). It scales nearly as $\Gamma^{1/2}$ (dashed line), or, since $g' \propto \Gamma$, it also scales as $g'^{1/2}$. The cyclonic transport around the island (triangles), on the other hand, scales linearly with Γ. Each of these are consistent with the QG scaling. Finally, the angle of the separation point of the dense and buoyant currents (Φ, defined as clockwise from the source region) was diagnosed as the location of maximum mean offshore velocity at the surface, relative to the location of dense water formation. This is found to be only weakly dependent on Γ, increasing slightly from about 1.3 to 1.8 radians (75° to 103°).

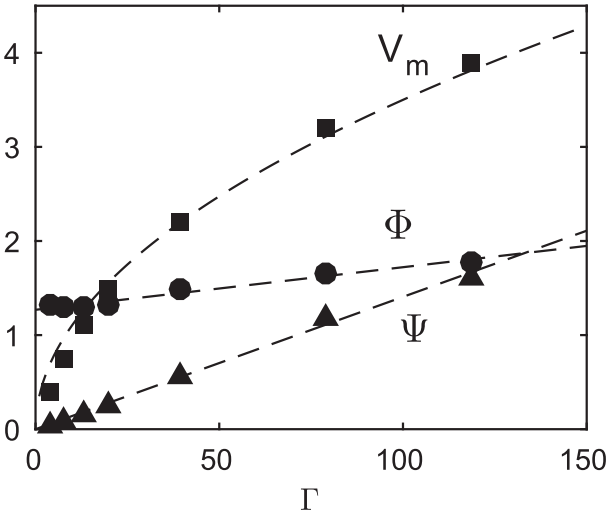

FIG. 7. Diagnostics from a series of numerical model runs for various Γ ($\text{W}\,\text{m}^{-2}\,^\circ\text{C}^{-1}$). Squares: maximum anticyclonic velocity at the surface along the eastern flank of the island ($\text{cm}\,\text{s}^{-1}$). Triangles: cyclonic transport around the island ($10^6\,\text{m}^3\,\text{s}^{-1}$). Circles: angle at which the dense plume flows offshore Φ (clockwise from the region of dense water formation). The dashed lines are linear fits for the angle and transport and proportional to $\Gamma^{1/2}$ for the maximum velocity.

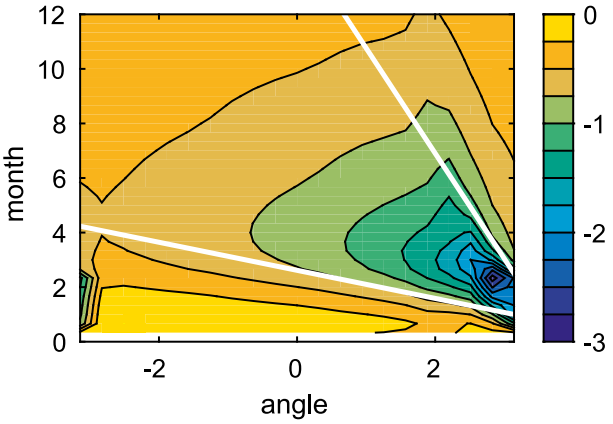

FIG. 8. Annual cycle of sea surface height anomaly within 10 km of the island boundary as a function of angle (source is at π, 0 is the eastern side of the island) and time (contour interval 0.25 cm). The two white lines mark phase speeds of 15 and 2 cm s^{-1} for reference.

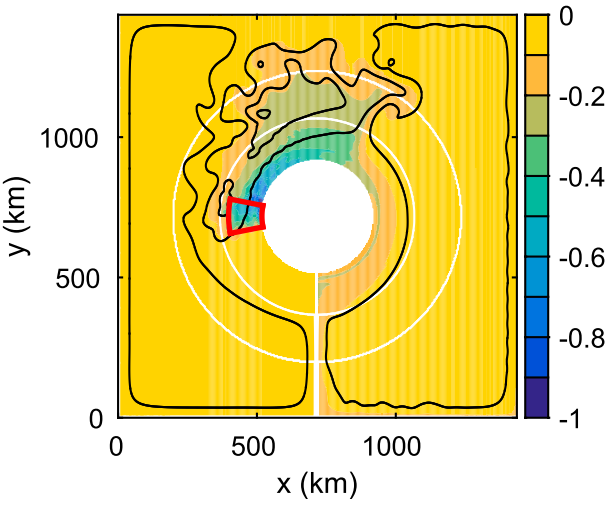

FIG. 9. Mean bottom temperature anomaly (colors), transport streamfunction (black contours, contour interval 0.1 Sv), and bottom topography (white contours depths 250 and 500 m) for a case with the same parameters as in Fig. 6 but with a narrow wall connecting the island to the southern boundary.

The cyclonic circulation around the island, in the linear limit, is barotropic. It results from the low sea surface height signal in the region of deep convection reaching the boundary of the island, where the pressure signal then propagates as a Kelvin or shelf wave anticyclonically around the island. Note that a similar wave would be supported by a rigid lid with variable pressure at the surface, as is represented in the QG model in section 2 (with infinite wave speed for QG physics). This propagation away from the dense water formation region is evident from the distribution of the sea surface height anomaly within 10 km of the island boundary, averaged into an annual cycle from each of the 10 years of model integration as a function of time and angle in Fig. 8. The sea surface height is lowest near the forcing region at the end of the forcing period. The signal propagates anticyclonically around the island with a range of phase speeds between approximately 2 and 15 cm s^{-1}, so the waves are dispersive. The fastest signal speed is well above any advective velocities in the system, so this must be transmitted by waves. The spreading of the low sea surface height signal leaves behind a depression near the island, which is largest at the boundary and decreases offshore. This results in a geostrophically balanced cyclonic flow around the island.

The importance of these waves for the setup of the mean circulation is demonstrated by a case with a narrow wall connecting the island to the southern boundary, as in Fig. 9. The circulation is now largely confined to the region of dense water formation and its descent downslope to the north. The cyclonic circulation is largely absent. If the development of the cyclonic circulation were simply by advection away from the forcing region, one would expect to see the cyclonic flow approach and then be deflected by the wall. Instead we do not see any significant flow approaching the wall from either side. Interestingly, the temperature anomaly is also smaller than for the case without the wall but it extends farther from the formation area. There is also a narrow band of slightly denser water flowing anticyclonically away from the formation region in shallow water. This is reminiscent of the shallow pathway discussed by Zhang and Cenedese (2014).

4. Laboratory experiments

a. *Experimental apparatus*

The laboratory experiments were conducted in a transparent Perspex tank of depth 42 cm and with a circular base of radius 50 cm. The tank was positioned on a 1-m-diameter rotating turntable with a vertical axis of rotation. A topographic feature was located in the center of the tank. The topography consisted of a plastic cylinder (9.5-cm diameter and 13-cm height) sealed to an axisymmetric sloping bottom (i.e., a cone) with slope $\alpha_T = 0.726$. The maximum height of the sloping bottom in the center of the tank was 14.5 cm, and the outer radius was 20 cm. Hereinafter, we will refer to the plastic cylinder as the ''island'' and the sloping topography as the ''continental slope'' (Fig. 10a).

The tank was filled with freshwater of density ρ_1, which was initially in solid body rotation. A reservoir

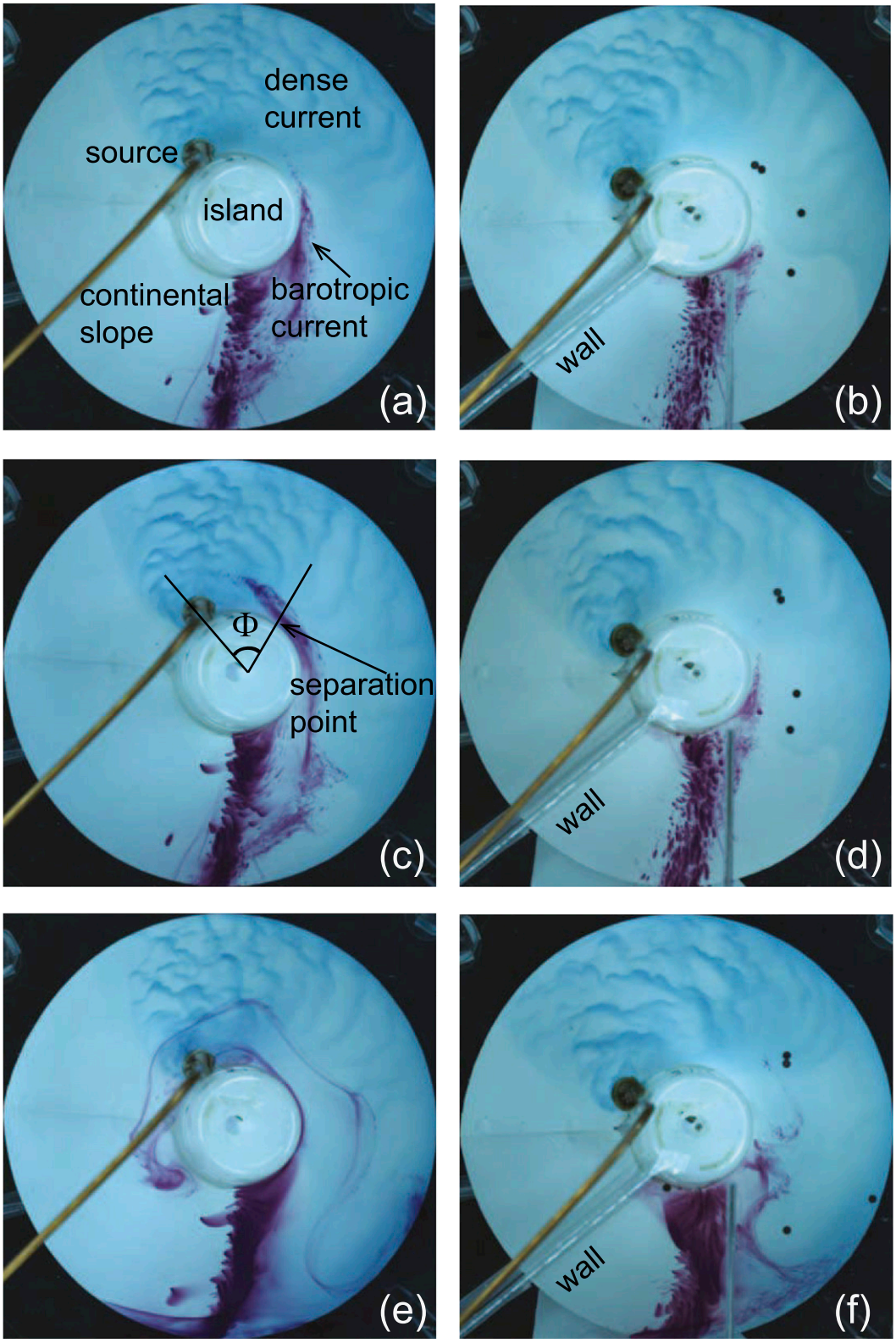

FIG. 10. Top view of the laboratory experiments. (left) An experiment with no wall; (right) an experiment with a radial wall present in the tank. The parameters are the same for both experiments: $H_s = 2\,\text{cm}$, $f = 1.4\,\text{s}^{-1}$, $Q = 1.4\,\text{cm}^3\,\text{s}^{-1}$, and $H_0 = 8\,\text{cm}$. (a),(b) Images taken $2.9T$ after the potassium permanganate crystals were dropped in the

of salted and dyed water of density $\rho_2 > \rho_1$ was placed on the rotating table and connected to a copper point source via a plastic tube and a pump. The source was covered with a sponge to minimize mixing between the dense and light fluids near the source, and it was positioned near the island, over the shallowest part of the tank (Fig. 10a), at a distance H_s above the sloping bottom. The ambient water height at the source location was $H_0 = 8$ cm and was kept constant for all experiments but one in which it assumed the value of 13 cm. The distance H_s assumed values of 0.5, 2, 3, 4, 5, 6, and 8 cm.

The buoyancy forces are described by the reduced gravity $g' = 2g(\rho_2 - \rho_1)/(\rho_2 + \rho_1)$, where g is the gravitational acceleration. In the experiments g' took values between 2 and 24 cm s^{-2}, and the Coriolis parameter was kept fixed at $f = 1.4$ s^{-1}. The flow rate through the source was held constant at $Q = 1.4$ cm^3 s^{-1}, with the exception of two experiments in which it assumed values of 3.5 and 5.4 cm^3 s^{-1}. The magnitude of the slope used in the laboratory experiments differs from typical values found in the ocean and used in the numerical simulations. However, the relevant parameter is the slope Burger number $(L_d\alpha_T)/H$, where L_d is the horizontal scale (i.e., the baroclinic deformation radius), H is the vertical scale, and α_T is the slope with the horizontal. In the laboratory, the slope Burger number ranges between 0.05 and 0.375, while in the numerical simulations, the slope Burger number ranges between 0.04 and 0.06. Hence, the numerical simulations and the laboratory experiments have values of the slope Burger number that overlap, although the laboratory experiments span a much larger range of values.

A total of 16 experiments were conducted. Each experiment started by switching on the pump and the video camera mounted above the tank and fixed to the turntable so that measurements could be obtained in the rotating frame of reference. The dense current was dyed using blue food coloring, and it was observed both from the top and side view. The ambient flow was observed by dropping potassium permanganate crystals along a radial section located between 180° and 270° clockwise around the island from the source location. Digital movies of the purple streaks left behind by the crystals were taken from the camera positioned above the tank (Fig. 10) and their analysis gives a measure of the ambient flow within the tank. The side view of the purple streaks (not shown) revealed that the streaks maintained a vertical position when the dense water plume was not present, an indication that vertical shear was absent away from the dense water. This differs from the numerical calculations in the previous section, where the cyclonic flow developed a cold bottom boundary layer and vertical shear in the azimuthal velocity. This is because the laboratory experiments were carried out in an unstratified ambient fluid, so the bottom Ekman layer does not advect dense water upslope, as found in the stratified numerical experiments, and thus does not result in a horizontal density gradient and vertical shear over the sloping bottom.

b. *Barotropic ambient flow*

The dense current was observed to descend the continental slope in a similar manner as observed in previous studies (e.g., Cenedese et al. 2004; Cenedese and Adduce 2008). The focus of the present experiments was on the flow established in the ambient fluid above and ahead of the dense current. After the dense current started to descend the slope, moving around the island in an anticyclonic direction, the ambient fluid was observed to move cyclonically around the island with a maximum azimuthal velocity V_θ located near the island, over the shallowest region in the tank (Fig. 10a). However, the barotropic ambient current was observed to separate from the island and move into deeper water at a location distant an angle Φ from the source (Fig. 10c). After the current detached from the island, it continued to move cyclonically around the topography (Fig. 10e).

One further experiment was conducted positioning a radial vertical wall approximately 45° from the source in the direction opposite to the propagation of the dense current (Fig. 10b). The wall prevented baroclinic and barotropic signals from propagating completely around the island. While the propagation of the bottom dense current was not drastically changed compared to the experiments where the wall was absent (Figs. 10a,b), the barotropic ambient flow was dramatically halted by the presence of the wall (Fig. 10f). During an initial transit time, a slower cyclonic motion was present around the island also when a radial wall was present (Fig. 10d). However, after approximately $9.3T$, where $T = 2\pi/\Omega$ is the rotation period of the table, the cyclonic motion was suddenly arrested and the ambient fluid did

←

tank, (c),(d) images after $4.4T$, and (e),(f) images after $11.1T$, where $T = 2\pi/\Omega$ is the rotation period of the table. The experiment with a wall in the right column used a plastic tray to distribute the potassium permanganate crystals along a radial section visible south of the island and east of the wall.

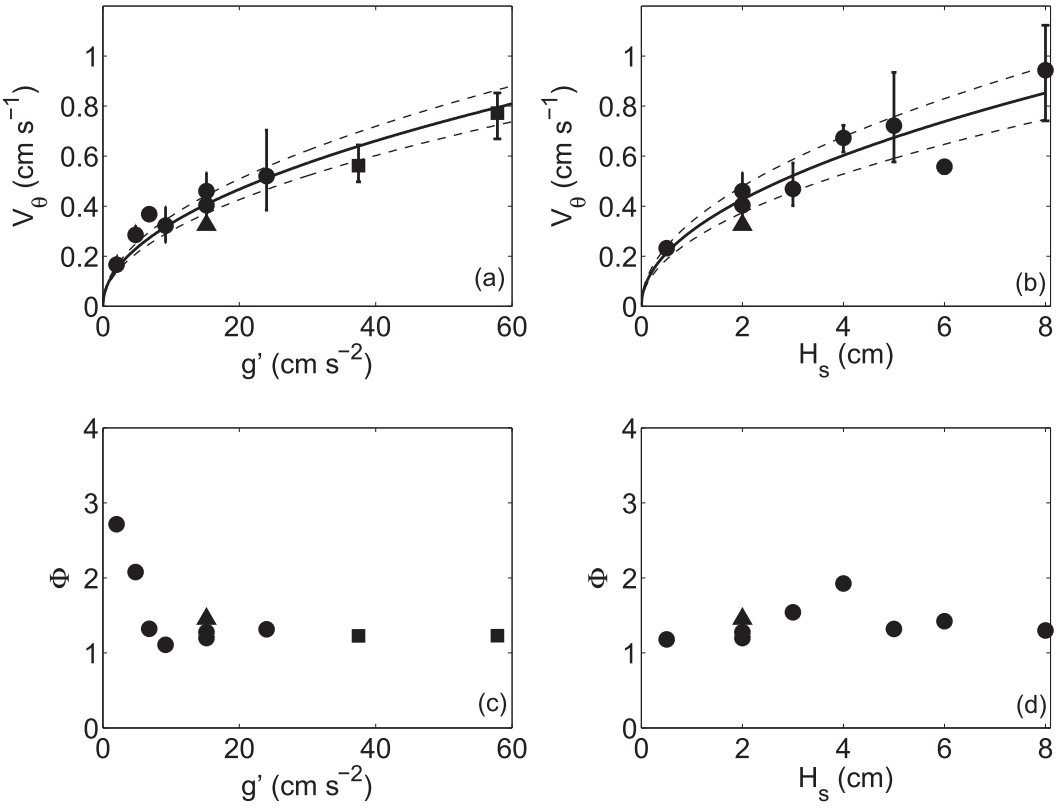

FIG. 11. The dependence of the maximum barotropic azimuthal velocity V_θ on (a) the reduced gravity g' and (b) source height H_s is well represented by a power law of 1/2 (solid black lines). The dashed lines represent the 95% confidence interval, and the R^2 value of the fit is (a) 0.91 and (b) 0.84. The angle at which the barotropic ambient flow detaches from the island is approximately independent of (d) H_s and (c) g', except for the lowest values of g'. Error bars are given by the maximum and minimum values of the velocity measurements. Square symbols represent experiments with a flow rate different than $Q = 1.4\,\mathrm{cm^3\,s^{-1}}$, while triangles represent the experiment with $H_0 = 13\,\mathrm{cm}$.

not present any organized cyclonic flow around the island (Fig. 10f).

The fact that the barotropic ambient flow is only observed in the absence of a radial wall suggests that this flow is a consequence of a signal that needs to propagate unconstrained around the island.

c. *Scalings*

The maximum barotropic azimuthal velocity increased with increasing values of the reduced gravity and source height above the bottom (Figs. 11a,b). The two experiments with a different flow rate were included in this comparison by assuming that the buoyancy flux $B = g'Q$ in the dense current is conserved, a classic assumption in plume theory (Morton et al. 1956). This assumption allowed us to obtain an equivalent reduced gravity given by $g' = g'^*Q^*/Q$, where g'^* is the reduced gravity for each of the two experiments having a different flow rate Q^* than the value $Q = 1.4\,\mathrm{cm^3\,s^{-1}}$. These two experiments are represented by the square symbols in Fig. 11, while the experiment with $H_0 = 13\,\mathrm{cm}$ is represented by the triangle.

The increase in velocity with both the reduced gravity and source height suggests that the barotropic flow is set up by a signal whose intensity is proportional to the baroclinic gravity wave speed $(g'H_s)^{0.5}$. This hypothesis is confirmed by Fig. 12, comparing the measured azimuthal velocity with the baroclinic gravity wave speed for experiments in which the reduced gravity (circles), the source height (squares), and the flow rate (triangles) were varied. The scaling of the maximum anticyclonic velocity with $g'^{1/2}$ is in agreement with the scaling obtained with the QG theory and numerical model.

The angle Φ from the source where the current is observed to detach from the island is approximately independent of g' and H_s (Figs. 11c,d), with the exception of the two experiments having the lowest g' for which the value of Φ is observed to increase with decreasing g' (Fig. 11c). The separation point is

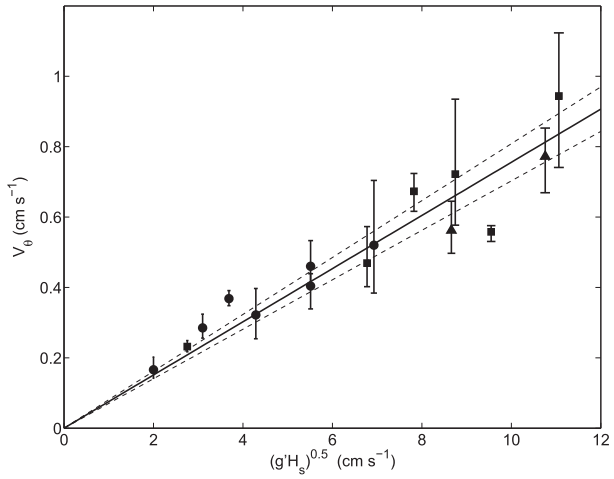

FIG. 12. The maximum barotropic azimuthal velocity V_θ scales with the baroclinic gravity waves speed $(g'H_s)^{0.5}$ as indicated by the linear fit (black solid line). The dashed lines represent the 95% confidence interval, and the R^2 value of the fit is 0.93. Error bars are given by the maximum and minimum values of the velocity measurements. Circles (squares) represent experiments in which $g'H_s$ was varied, and triangles experiments with a flow rate different than $Q = 1.4\,\text{cm}^3\,\text{s}^{-1}$.

typically 77° clockwise from the source, which is similar to that found in the numerical model.

5. Summary

The large-scale circulation along closed topographic contours resulting from localized buoyancy forcing is explored using quasigeostrophic theory, a nonlinear primitive equation model, and rotating tank experiments. In addition to the dense bottom plume that flows anticyclonically from the source region, which has received much previous attention, we find that the flow is dominated by a cyclonic circulation that flows along the topographic contours all the way around the topographic feature. Even though the technical details and parameter ranges for each approach differs, this circulation feature is prominent in all cases. Since this flow is set up by the rapid propagation of barotropic waves, it is expected that similar patterns will be found even for planetary-scale topographic features. For sufficiently strong forcing there exists a region of confluence between the anticyclonic dense water plume and the cyclonic circulation that forces an abrupt offshore flow of both dense water at the bottom and buoyant water at the surface. The quasigeostrophic theory, numerical simulations, and laboratory experiments all suggest that the maximum cyclonic velocity scales with $g'^{1/2}$, while the angle of detachment of the dense water and buoyant water found in the model and laboratory is typically 80° clockwise from the source and only weakly dependent on the forcing parameters.

Acknowledgments. MAS was supported by the National Science Foundation under Grant OCE-1534618. CC would like to thank Anders Jensen for the able assistance in the laboratory. Support for CC was given by the WHOI Ocean Climate Change Institute Proposal 27071273.

REFERENCES

Cenedese, C., and C. Adduce, 2008: Mixing in a density-driven current flowing down a slope in a rotating fluid. *J. Fluid Mech.*, **604**, 369–388, doi:10.1017/S0022112008001237.

——, J. A. Whitehead, T. A. Ascarelli, and M. Ohiwa, 2004: A dense current flowing down a sloping bottom in a rotating fluid. *J. Phys. Oceanogr.*, **34**, 188–203, doi:10.1175/1520-0485(2004)034<0188:ADCFDA>2.0.CO;2.

Danielson, S., K. Aagaard, T. Weingartner, S. Martin, P. Winsor, G. Gawarkiewicz, and D. Quadfasel, 2006: The St. Lawrence polynya and the Bering shelf circulation: New observations and a model comparison. *J. Geophys. Res.*, **111**, C09023, doi:10.1029/2005JC003268.

Marshall, J., and F. Schott, 1999: Open-ocean convection: Observations, theory, and models. *Rev. Geophys.*, **37**, 1–64, doi:10.1029/98RG02739.

——, C. Hill, L. Perelman, and A. Adcroft, 1997: Hydrostatic, quasi-hydrostatic, and nonhydrostatic ocean modeling. *J. Geophys. Res.*, **102**, 5733–5752, doi:10.1029/96JC02776.

Moore, G. W. K., and R. S. Pickart, 2012: The Wrangle Island polynya in early summer: Trends and relationships to other polynyas and the Beaufort Sea high. *Geophys. Res. Lett.*, **39**, L05503, doi:10.1029/2011GL050691.

Morton, B. R., G. Taylor, and J. S. Turner, 1956: Turbulent gravitational convection from maintained and instantaneous sources. *Proc. Roy. Soc. London*, **A234**, 1–23, doi:10.1098/rspa.1956.0011.

Pedlosky, J., 1987: *Geophysical Fluid Dynamics*. 2nd ed. Springer-Verlag, 710 pp.

Skogseth, R., L. H. Smedsrud, F. Nilsen, and I. Fer, 2008: Observations of hydrography and downflow of brine-enriched shelf water in the Storfjorden polynya, Svalbard. *J. Geophys. Res.*, **113**, C08049, doi:10.1029/2007JC004452.

Spall, M. A., 2004: Boundary currents and water mass transformation in marginal seas. *J. Phys. Oceanogr.*, **34**, 1197–1213, doi:10.1175/1520-0485(2004)034<1197:BCAWTI>2.0.CO;2.

——, 2013: Dense water formation around islands. *J. Geophys. Res. Oceans*, **118**, 2507–2519, doi:10.1002/jgrc.20185.

Visbeck, M., J. Marshall, and H. Jones, 1996: Dynamics of isolated convective regions in the ocean. *J. Phys. Oceanogr.*, **26**, 1721–1734, doi:10.1175/1520-0485(1996)026<1721:DOICRI>2.0.CO;2.

Welander, P., 1968: Wind-driven circulation in one- and two-layer oceans of variable depth. *Tellus*, **20**, 1–16, doi:10.1111/j.2153-3490.1968.tb00347.x.

Young, W. R., and P. B. Rhines, 1982: A theory of the wind-driven circulation. II. Gyres with western boundary layers. *J. Mar. Res.*, **40**, 849–872.

Zhang, W. G., and C. Cenedese, 2014: The dispersal of dense water formed in an idealized coastal polynya on a shallow sloping shelf. *J. Phys. Oceanogr.*, **44**, 1563–1581, doi:10.1175/JPO-D-13-0188.1.